ELSEVIER

Journal of Structural Geology 27 (2005) 1741–1749

JOURNAL OF STRUCTURAL GEOLOGY

www.elsevier.com/locate/jsg

Evidence for regional Dauphiné twinning in quartz from the Santa Rosa mylonite zone in Southern California. A neutron diffraction study

J. Pehl, H.-R. Wenk*

Department of Earth and Planetary Science University of California, Berkeley, CA 94720, USA

Received 23 February 2005; received in revised form 25 May 2005; accepted 1 June 2005
Available online 16 August 2005

Abstract

Preferred orientation in granitic mylonites from the Santa Rosa mylonite zone in Southern California is investigated with time-of-flight neutron diffraction. Quartz and biotite display strong preferred orientation, whereas, feldspar alignment is weak. For quartz, a *c*-axis maximum in the intermediate fabric direction is consistent with dynamic recrystallization. Pole figures for positive and negative rhombs, such as $r=\{10\bar{1}1\}$ and $z=\{01\bar{1}1\}$, are distinct over a wide region, suggesting that the pattern reflects tectonic deformation and was not affected by local late-stage mechanical Dauphiné twinning. Indeed, modeling based on the elastic properties of quartz indicates that compression perpendicular to the foliation may have induced Dauphiné twinning and this mechanism may thus be useful as a paleo-piezometer to record tectonic stresses in quartz-bearing rocks.

Keywords: Quartz; Texture; Dauphiné twinning; Mylonites; Neutron diffraction; Paleo-piezometer

1. Introduction

Mechanical twinning has been used in calcite as a paleo-piezometer (e.g. Groshong et al., 1984; Rowe and Rutter, 1990). Trigonal α-quartz also undergoes mechanical twinning to form Dauphiné twins (Schubnikow and Zinserling, 1932; Thomas and Wooster, 1951). Dauphiné twins, which also occur as growth twins and are associated with the α–β quartz transition, are related by a 180° rotation about the *c*-axis (equivalent to a 60° rotation in trigonal quartz) and have the same handedness, unlike Brazil twins. Twinning involves only small atomic displacements and does not change the orientation of the *c*-axis. However, it transposes positive rhombs (e.g. $10\bar{1}1$) and negative rhombs (e.g. $01\bar{1}1$) and reverses the orientation of the polar *a*-axes. Dauphiné twinning is also called electrical twinning for its effect on piezoelectric properties (Wooster and Wooster, 1946).

Compression experiments on polycrystalline quartz showed that significant Dauphiné twinning occurred at stresses of 200–1500 MPa (Tullis, 1970; Tullis and Tullis, 1972). But, while preferred orientation of quartz has been the subject of numerous studies, very few investigations have explored the trigonal crystal symmetry in natural quartz textures. With the petrographic microscope, only the *c*-axis can be measured and Dauphiné twins are invisible. Only with diffraction methods can the trigonal symmetry be resolved, based on intensity differences between positive and negative rhombs (e.g. for neutrons 72% for $10\bar{1}1$ and 28% for $01\bar{1}1$). With X-ray pole figure goniometry (e.g. Baker and Wenk, 1972; Baker and Riekels, 1977; Schmid and Casey, 1986), neutron diffraction (e.g. Helming et al., 1994), as well as electron backscatter diffraction (EBSD) (e.g. Heidelbach et al., 2000; Lloyd, 2000, 2004; Lloyd and Kendall, 2005) distinct differences in the orientation distribution of positive and negative rhombs in metamorphic quartz-bearing rocks could be documented, but this was never explored systematically. T. Tullis (1980) suggested that the ease of Dauphiné twinning would make it subject to post-tectonic stresses and thus render the trigonality of quartz useless for petromechanical interpretations.

Making use of the new opportunities for quantitative texture analysis with time-of-flight (TOF) neutron diffraction and data analysis with the Rietveld method, we decided

* Corresponding author. Fax: +1 510 643 9980.
E-mail address: wenk@seismo.berkeley.edu (H.-R. Wenk).

0191-8141/$ - see front matter © 2005 Elsevier Ltd. All rights reserved.
doi:10.1016/j.jsg.2005.06.008

to undertake a systematic study of quartz-bearing mylonites to explore the importance of trigonality in quartz textures and implications for Dauphiné twinning. Rather than pure quartzites we chose granitic mylonites for this investigation because of their widespread occurrence and tectonic significance. A previous neutron diffraction study described the evolution of texture as granodiorite is progressively deformed to mylonite and phyllonite (Wenk and Pannetier, 1990), but only with modern methods of spectral data analysis has it become possible to determine quantitative orientation distribution functions (ODF) of such complex polymineralic rocks. With fast measuring times at the HIPPO (HIgh pressure, Preferred Orientation) diffractometer at the Los Alamos Neutron Science Center (LANSCE), a series of samples can now be measured efficiently.

2. Sample description

Samples were collected from the Santa Rosa mylonite zone in Southern California (Fig. 1). This region forms the eastern margin of the Peninsular Ranges Batholith. The composition of the mylonites is granodioritic; quartz and plagioclase are the dominant minerals with a significant fraction (~10%) of biotite and 6–14% alkali feldspar (O'Brien et al., 1987). In thin section, the seven samples have similar microstructures. Large (up to 2 mm) crystals of feldspar are surrounded by a fine-grained groundmass (50–100 μm) (Fig. 2). Biotite grains in the groundmass appear strongly aligned and fine-grained quartz also shows preferred orientation as ascertained with the petrographic

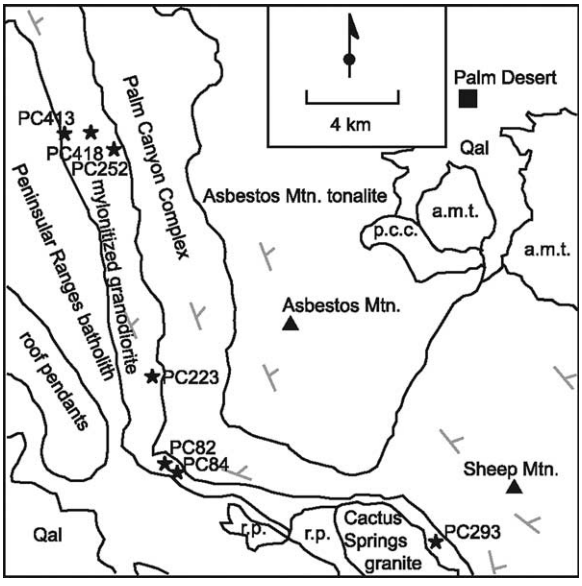

Fig. 1. Map of the Santa Rosa mylonite zone (based on Wenk and Pannetier, 1990). Stars within the mylonite zone indicate sample collection points. Gray symbols indicate foliation and lineation. Abbreviations: r.p., roof pendants; a.m.t., Asbestos Mountain tonalite; p.c.c., Palm Canyon Complex; Qal, Quaternary alluvium.

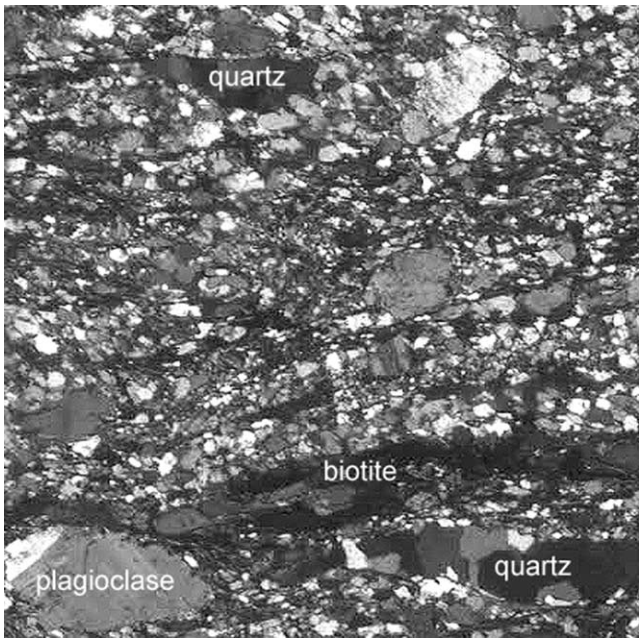

Fig. 2. Photomicrograph of PC 418, crossed polars. Width is 4 mm. Section is normal to the foliation plane and contains the lineation.

microscope. Previous studies revealed extensive recrystallization of quartz as well as biotite (Goodwin and Wenk, 1995).

The region was deformed in the late Cretaceous, resulting in a transition from undeformed granodiorite to mylonite and locally phyllonite and ultramylonite (Erskine and Wenk, 1985). Deformation occurred in amphibolite facies below the α–β quartz transition. Large strains were recorded in highly deformed enclaves (typically $\varepsilon = 1.5$–3), mainly due to flattening and accompanied by a top-to-the-west shear (Wenk, 1998). The mylonite shows a strong east-dipping foliation and an east-plunging lineation. The foliation and lineation directions were used to define a sample coordinate system for the seven specimens chosen for this study. Oriented samples were collected over 25 km (Fig. 1). Cylinders, 1 cm long and 0.8 cm in diameter, were drilled from each sample with the cylinder axis perpendicular to the foliation plane. The lineation direction was marked on the cylinder for reference. These cylinders were used for the neutron diffraction study with no further surface preparations required.

3. TOF neutron diffraction method

The samples were measured on the HIPPO TOF neutron diffractometer at LANSCE. Neutron diffraction is the optimal method for studying textures of polyphase materials with complex diffraction spectra. Due to low attenuation, neutrons sample bulk specimens, rather than thin surfaces and provide better statistics than X-ray pole figure goniometry or EBSD. With TOF measurements of

polychromatic neutrons, every detector records a continuous spectrum that includes many diffraction peaks (Fig. 3). The HIPPO diffractometer was designed for texture measurements, with 30 detectors arranged in three rings that cover nearly one quarter of the pole figure space (Matthies et al., 2005). The sample was rotated about the cylinder axis into six positions to increase the coverage, resulting in $6\times30=180$ spectra. The coverage is shown in Fig. 4. Each measurement takes 10–20 min, thus the total time for one sample is 1–2 h. Details of the HIPPO diffractometer and procedures for texture analysis have been described by Wenk et al. (2003) and Matthies et al. (2005).

4. Data analysis

Data analysis was performed with the Rietveld method as implemented in the software package MAUD (Materials Analysis Using Diffraction; Lutterotti et al., 1999). MAUD couples Rietveld analysis of crystallographic parameters (Young, 1993) with quantitative texture analysis. This powerful technique is able to separate the intensity contributions from overlapped peaks and analyze the texture of multiple phases simultaneously. MAUD fits the diffraction data by refining values for parameters describing the crystallography, experimental setup, and background. We used initial crystallographic parameters for quartz from Glinnemann et al. (1992) (spacegroup $P3_121$), for andesine

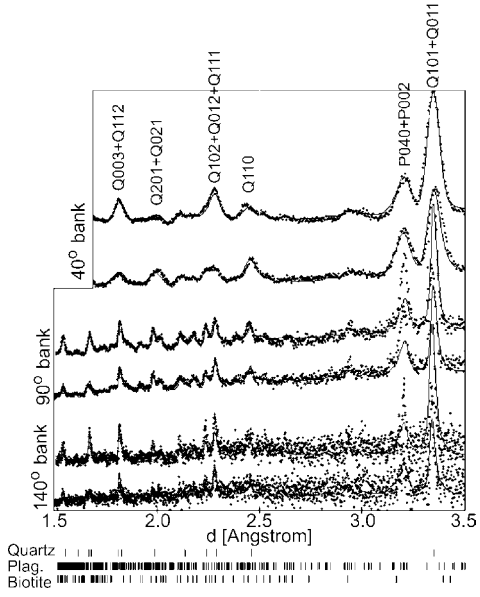

Fig. 3. Two TOF spectra for sample PC418 from each detector ring. One spectrum is near the lineation direction *X* and one closer to the pole of foliation *Z*. The *d*-axis reflects the computation range used for each bank. Locations of diffraction peaks for the three phases, quartz, plagioclase, and biotite, are plotted at the bottom. Indices for major peaks are noted (P, plagioclase; Q, quartz). Points are measured data; the solid line is the recalculated spectrum. Relative intensity differences between the two spectra are due to texture.

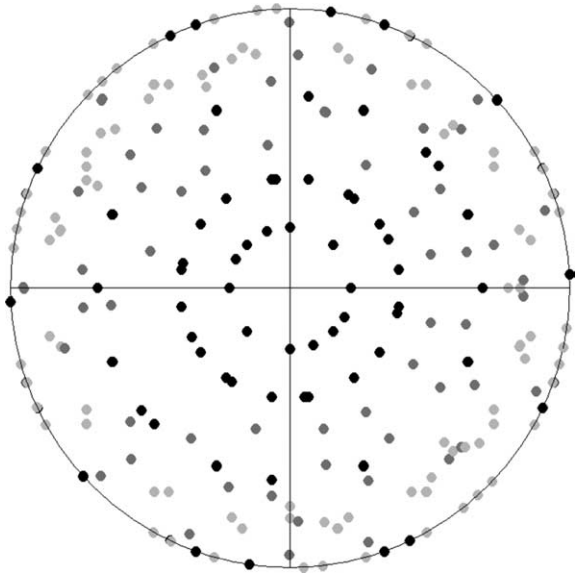

Fig. 4. Pole figure coverage. Sample was rotated about the cylinder axis (which was vertical) to 0, 45, 90, 135, 202.5, and 242°. Thirty detector panels on three rings at different Bragg angles were used. 140° ring, light gray; 90° ring; gray, 40° ring; black.

from Gerald et al. (1986 (spacegroup $C\bar{1}$), and biotite from Brigatti and Davoli (1990) (spacegroup $C12/m$). Atomic coordinates and temperature factors were kept constant during the analysis, lattice parameters were refined.

A few comments are pertinent about the structure of quartz since there is some confusion in the literature. Quartz exists in right- and left-handed forms, which belong to spacegroups $P3_121$ and $P3_221$. The two forms are indistinguishable by normal diffraction methods. For right- as well as for left-handed forms, $10\bar{1}1$ neutron diffractions have a higher intensity than those from $01\bar{1}1$, $10\bar{1}1$ corresponding to the morphologically dominant positive rhomb *r*, which is close to the elastically softest direction, as we shall see later. Note that this is not the case for the structure reported by Will et al. (1988). We performed calculations both for right- and left-handed quartz. The left-handed form is generated from the right-handed structure by inverting the coordinates through the origin and reversing the sense of the screw axis from 3_1 to 3_2. Results are the same for both forms, i.e. handedness does not affect our conclusions about texture and Dauphiné twinning. Quartz-bearing rocks contain both right- and left-handed crystals and a model consisting of equal numbers of the two forms produces the same results as one using only one of the two forms. In most quartzites that have been investigated for handedness, an equal number of left- and right-handed crystals was observed (Wenk, 1985, p. 30).

The 180 diffraction spectra are divided into three data sets corresponding to the three rings of detectors. They are used simultaneously in the Rietveld refinement. The computation range is selected for each data set based on the resolution of the detector and the locations of important

diffraction peaks. For these samples, computation ranges were 1.5–3.5 Å (140° and 90° bank) and 1.7–3.5 Å (40° bank). The minimum d-spacings used in the computation were chosen to avoid regions with too many overlaps. Fig. 3 shows two sample spectra from each dataset, one in the vicinity of the Z sample direction and the other in the vicinity of the X direction. The presence of texture can be seen by the variation in relative peak heights between the two spectra from the same bank. Note the difference in d-resolution between low- and high-angle detector banks.

Instrumental parameters for HIPPO have been determined by measurements of a standard. For initial relative phase proportions we used values given by Wenk and Pannetier (1990). The analysis proceeds in three stages. First the background and overall intensity of the spectra are fit into two steps. (a) The incident intensity and four background parameters for each spectrum are refined. (b) The incident intensity is fixed and a scale factor is refined for each detector panel to account for differences in detector efficiency. Second, to fit the locations of the diffraction peaks, lattice parameters are included in the refinement along with two parameters describing the displacement of the sample from the position calibrated with the standard. Finally, the shape of the diffraction peaks is modeled by including the average isotropic grain size of quartz (width) and phase fraction of quartz and biotite (height relative to other phases). The phase fraction of plagioclase was calculated such that the three phases totaled one. Texture is responsible for changes in the relative heights of peaks within a phase and texture analysis is also included in the third stage.

From the measured spectra, the integrated intensity (area under the peak) is computed by the LeBail method (LeBail et al., 1988) and passed to the texture algorithm to calculate the ODF. We choose the WIMV-based (Williams–Imhof–Matthies–Vinel; Matthies and Vinel, 1982) algorithm E-WIMV that allows for data in arbitrary positions (Matthies, 2002). Using direct methods, E-WIMV calculates a discrete ODF for the specified phases. The discretization is controlled by specifying a grid size for the ODF and a projection tube radius. Because quartz has a strong texture and is of primary interest in this study, a grid size of 10° was used, while for plagioclase and biotite a larger grid size of 15° was applied. Correspondingly projection tube radii are 20° and 30°, respectively. A coupled Rietveld-texture refinement is then performed in three cycles. The ODF for each phase has been exported from MAUD and smoothed with a 7.5° Gauss filter in the program Beartex (Wenk et al., 1998) to remove stochastic effects between grid cells in the discrete ODF and, if necessary, to perform rotations. From this transformed ODF various pole figure have been calculated, even for diffraction peaks that are overlapped in the spectra, such as positive and negative rhombs of quartz.

5. Results

Fig. 3 shows examples taken from the 180 measured spectra (dots) for sample PC418. The Rietveld fit (line) is considered satisfactory, for position, shape and intensity. Obviously counting statistics are not optimal for 90° and 140° banks, but a compromise had to be made between counting time and number of samples to be measured.

Table 1 lists volume fractions and texture information for the seven samples. Provided is the texture index F_2 for each phase (Bunge, 1982), the ODF maximum (in multiples of a random distribution, m.r.d.) and the (001) maximum for quartz and biotite. The seven samples have similar composition with quartz making up 29–45% by volume and biotite 8–15%. The fraction of plagioclase was set so that the total volume of the three phases equaled 100%.

Texture information for biotite and quartz is displayed in pole figures that were recalculated from the ODF (Figs. 5 and 6). Plagioclase textures are weak, even before smoothing (Table 1), and pole figures are not shown. Pole

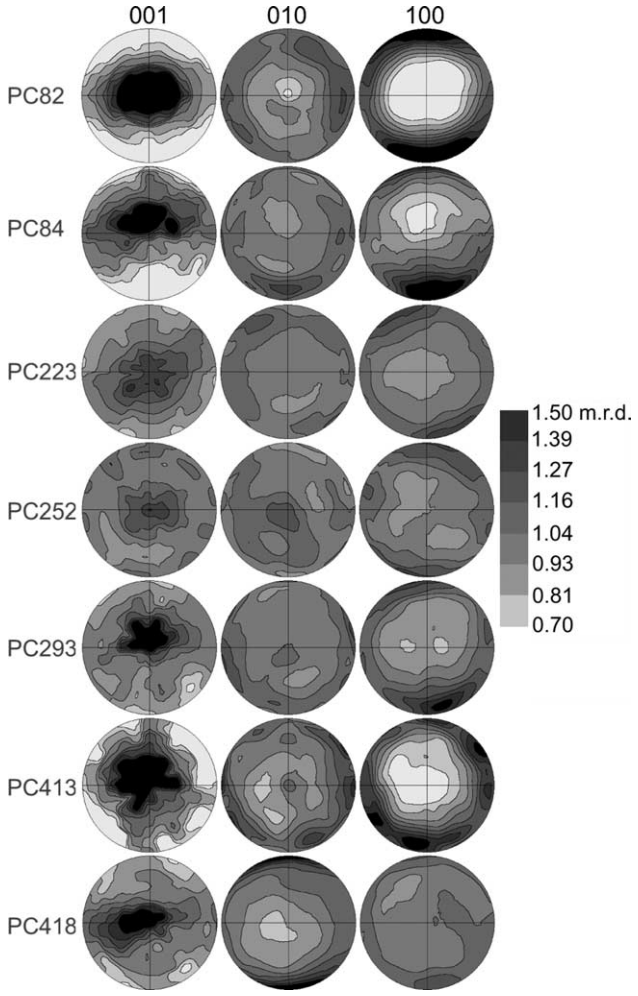

Fig. 5. Pole figures of biotite. Equal area projection, linear contour scale. Lineation direction (X) is NS, foliation normal (Z) at center, intermediate direction (Y) EW.

Table 1
Volume fractions and texture information (in multiples of a random distribution) for quartz, plagioclase, and biotite as determined by the Rietveld program MAUD

	PC 82	PC 84	PC 223	PC 252	PC 293	PC 413	PC 418
Vol% quartz	40.2	39.2	29.0	43.5	34.2	37.6	37.8
Vol% plagioclase	49.7	52.1	59.9	48.7	50.7	49.3	50.6
Vol% biotite	10.1	8.7	11.1	7.7	15.1	13.1	11.6
F_2 quartz	4.03	2.22	1.96	3.27	1.24	2.87	3.10
F_2 biotite	1.28	1.13	1.03	1.04	1.07	1.20	1.07
F_2 plagioclase	1.16	1.06	1.06	1.05	1.04	1.12	1.14
ODF max quartz	18.97	10.04	7.55	12.73	4.72	29.34	14.60
ODF max biotite	4.22	3.40	1.73	2.05	2.87	4.10	2.46
001 max quartz	7.93	5.57	4.63	8.00	2.89	5.76	7.65
001 max biotite	2.60	2.50	1.40	1.38	2.08	2.52	1.95

Volume fractions are given to the last significant digit as determined by MAUD. Actual uncertainties may be considerably higher.

figures are projected onto the foliation plane (X–Y) and the lineation direction (X) is vertical. Z is the normal to the foliation plane (center of pole figure).

5.1. Biotite

Fig. 5 shows pole figures of biotite for each of the seven samples. Though there is variation in texture strength, the 001 texture maximum is for all samples centered around Z, the normal to the foliation plane. The maximum is elongated in the plane normal to the lineation (YZ). The 100-pole figure shows concentrations in the XY plane with a weak maximum parallel to the lineation. This pattern agrees with previous results by O'Brien et al (1987) and Wenk and Pannetier (1990). However, the strength of the biotite texture is surprisingly weak. The previous studies documented

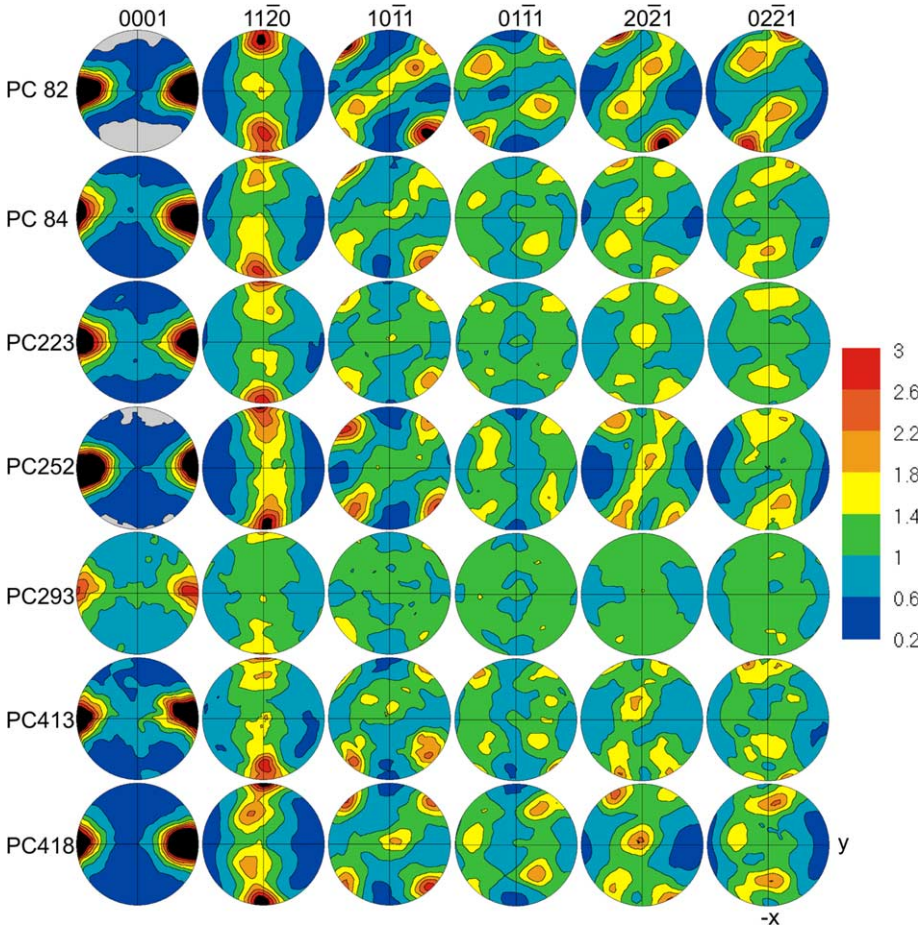

Fig. 6. Pole figures of quartz. Equal area projection, linear contour scale. Lineation direction (X) is NS, foliation normal (Z) at center, intermediate direction (Y) EW.

001-pole figures with strengths in excess of 12 m.r.d. We attribute the discrepancy to limitations of the Rietveld procedure in this case. The strong basal biotite reflections that are most distinct are outside the d-spacing range that can be recorded by TOF neutrons with HIPPO. We consider the biotite texture at the limits of what is resolvable with this technique; still the overall texture pattern is reasonable and consistent.

5.2. Quartz

Fig. 6 shows pole figures of the *c*-axis (0001), *a*-axes $\{11\bar{2}0\}$, positive and negative unit rhombs $\{10\bar{1}1/01\bar{1}1\}$, and positive and negative $\{20\bar{2}1/02\bar{2}1\}$ rhombs. Though the absolute texture strength varies (Table 1), all samples have similar texture patterns. The 0001 pole figure shows a strong maximum in the intermediate fabric direction *Y*. The $11\bar{2}0$ pole figures display a great circle girdle around *Y* with a maximum in the lineation direction *X*. These results are consistent with those of Wenk and Pannetier (1990), whose sample PC 82 was included in this study. The symmetry of 0001 and $11\bar{2}0$ pole figures is approximately orthorhombic.

Pole figures for positive and negative rhombs are less symmetrical than those for *c*- and *a*-axes. There is approximately a 2-fold rotation axis at *Z* but there are no mirror planes. For $10\bar{1}1$ there is a maximum at NW (SE) and a girdle extending from SW to NE with maxima at SW and NE. The $01\bar{1}1$ pole figures are less distinct and have no distinct maxima on the periphery. Clearly the pole figures for positive and negative rhombs are different. The $20\bar{2}1$ pole figures have maxima near the center (*Z*) and pairs of maxima on the periphery to the left and right of *X*. For $02\bar{2}1$, maxima are in the *X* direction, but for the most part are not on the periphery. It is impressive to note how consistent the pole figures are for different samples, even for the rhomb planes.

6. Interpretation

The quartz texture with a *c*-axis maximum in the intermediate fabric direction is typical of high temperature mylonites and figures already prominently in Sander's (1950) classical book. Since then, it has been described by many investigators. It appears to be typical for dynamically recrystallized rocks. This texture type cannot be explained with the best established slip systems for quartz, basal $(0001)<11\bar{2}0>$ and prismatic $\{10\bar{1}0\}[0001]$ or $\{10\bar{1}0\}<\bar{1}2\bar{1}0>$, but has plausibly been interpreted with a dynamic recrystallization model that emphasizes nucleation of the most heavily deformed orientations and corresponding growth of those nuclei (Wenk et al., 1997; Takeshita et al., 1999). The orthorhombic 0001 and 11-20 pole figure symmetry indicates a dominantly co-axial strain path, rather than simple shear.

Neither basal and prismatic slip systems nor the recrystallization model explain the difference between pole figures of positive and negative rhombs, nor their monoclinic pole figure symmetry. There are two possibilities: conceivably there are rhombohedral slip systems, but they have not been established experimentally with single crystals, nor by identification of corresponding dislocations in polycrystals. Evidence for such slip systems is thus circumstantial (Schmid et al., 1981).

A second possibility is activation of mechanical Dauphiné twinning and in the following discussion we will emphasize this mechanism. Mechanical Dauphiné twinning occurs in response to stress. In a quartz aggregate with random texture, application of an axial compressive stress creates preferred orientation of the rhomb planes, while maintaining a random distribution of *a*- and *c*-axes, without significant macroscopic deformation of the sample (Tullis, 1970). Repeated experiments (Tullis and Tullis, 1972) demonstrated that the induced texture consistently formed with the poles of the $\{10\bar{1}1\}$ planes parallel to the compression direction and $\{01\bar{1}1\}$ poles on small circle girdles at 30° to the compression direction.

Thomas and Wooster (1951) developed a theory of 'piezocrescence' to explain the growth of one twin orientation over another due to applied stress. They found that twinning would act to maximize elastic strain energy. For an axial stress, the change in elastic strain energy upon twinning, ΔW, can be expressed as

$$\Delta W = 1/2[(1/E_{\text{twin}})-(1/E_{\text{o}})](\sigma_1-\sigma_3)^2$$

where E_{o} and E_{twin} are stiffnesses for host and twin, respectively, in the compression direction and $\sigma_1-\sigma_3$ is the differential stress (Tullis and Tullis, 1972). In the case of an axial stress, the differential stress is the same for both twin variants and twinning causes grains with stiff directions parallel to an applied stress to twin to softer directions. Fig. 7 plots the stiffness surface of α-quartz (Young's modulus) relative to crystal coordinates, based on the isothermal elastic properties of McSkimin et al. (1965).

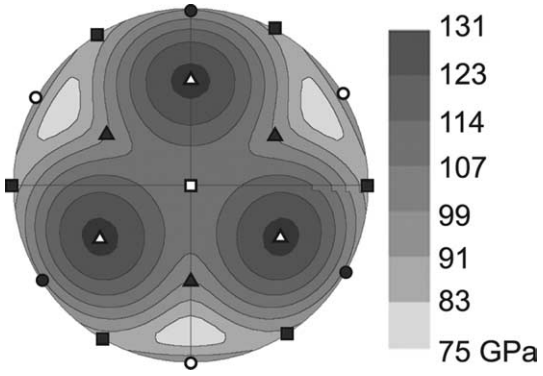

Fig. 7. Young's modulus of quartz projected on a sphere with crystal coordinates indicated. Calculated using isothermic elastic constants of McSkimin et al. (1965). Linear scale, equal area projection. White square, {0001}; black squares, $\{11\bar{2}0\}$; white circles, $\{10\bar{1}0\}$; black circles, $\{01\bar{1}0\}$; white triangles, $\{01\bar{1}1\}$; black triangles, $\{10\bar{1}1\}$.

Clearly this surface is very anisotropic with stiffest directions (near $02\bar{2}1$) with 131 GPa, and softest directions (near $10\bar{1}1$) with 75 GPa. Orientations with high stiffness such as $01\bar{1}1$ and $02\bar{2}1$ will twin to align weaker directions such as $10\bar{1}1$ and $20\bar{2}1$ with the direction of maximum stress.

We can use this concept for a model. We begin with 5000 random orientations, each specified by three Euler angles φ_1, Φ, φ_2 (Bunge, 1982). Next, we apply Dauphiné twinning to each orientation, thus generating 5000 new orientations φ_1, Φ, $\varphi_2 + 180°$, since Dauphiné twinning corresponds to a 2-fold rotation about the crystal *c*-axis. The 10,000 discrete orientations are then transformed in Beartex to a continuous ODF first entering them into discrete $5° \times 5° \times 5°$ ODF cells (program INOR) and then applying a 7.5° Gauss filter (program SMOO). The recalculated pole figures are essentially random (Fig. 8a). Next, we impose an axial stress to the center of the pole figure (*Z*). In the model, each of the 10,000 orientations selects the twin variant with the lower stiffness value. To account for incomplete twinning, a probability function is introduced, analogous to twinning models in polycrystal plasticity simulations (Tome et al., 1991). The stiffness ratio (difference divided by the maximum possible difference) is multiplied with a random number between 0 and 1. If the resulting product is greater than 0.25, then the orientation switches to its twin variant. Out of 10,000 orientations, 1533 orientations twin and the resulting distribution (Fig. 8b) has a maximum in the center of the $10\bar{1}1$ pole figure and a minimum in the center of the $01\bar{1}1$ pole figure, just as found by Tullis and Tullis (1972) and shown in Fig. 8c for a new experimentally compressed sample measured with neutron diffraction (Wenk et al., 2005). The 0001 and $11\bar{2}0$ pole figures do not change (Fig. 8a and b).

Now we use a similar approach for the textured mylonites. We choose PC 418 as an example and rotate the texture very slightly around *X* to improve the symmetry (Fig. 9a). Next, we take the same 5000 random orientations as before, but weigh each orientation according to the ODF value of the textured sample (Fig. 9b; this is done with program ODFW in Beartex). As before we twin each orientation and produce 10,000 orientations. Pole figures for positive and negative rhombs produced from this ODF are identical and have orthorhombic symmetry (Fig. 9c). Next, a compressive stress perpendicular to the foliation plane (*Z*, center of pole figure) is applied. In this case 1574 orientations twin and corresponding pole figures are shown in Fig. 9d. As is apparent, there is a strong similarity with the starting texture (Fig. 9b), with $10\bar{1}1$ concentrations on the periphery. Thus the observed texture can be explained largely by Dauphiné twinning. However, note that the model texture (Fig. 9d) has orthorhombic symmetry, whereas the measured texture is monoclinic. Obviously our assumption of axial compression perpendicular to the foliation is not strictly true, presumably because of an asymmetric simple shear component.

The same procedure that we applied to PC 418 could be applied to all other mylonite samples and, since the textures are very similar, we expect similar results. We want to emphasize again the similarity of the differences between $10\bar{1}1$ and $01\bar{1}1$ pole figures for all samples that we attribute to Dauphiné twinning. It indicates that the stress geometry that produced twinning was fairly homogeneous over a wide area and thus likely related to the tectonic strain field. Interestingly, the enclave study of Wenk (1998) inferred that the deformation in the region was caused predominantly by flattening and thus compression normal to the foliation is plausible. If Dauphiné twinning was caused by post-tectonic stresses such as during brittle faulting, seismic stresses associated with a nearby pseudotachylite zone (Wenk et al., 2000), or the adjacent San Jacinto and San Andreas faults, or even to stresses inflicted during sample excavation, then we would expect a much more heterogeneous pattern with great local variations in pole figures of positive and negative rhombs. Thus, looking at the results of this investigation, we are more optimistic than T. Tullis (1980) and think that

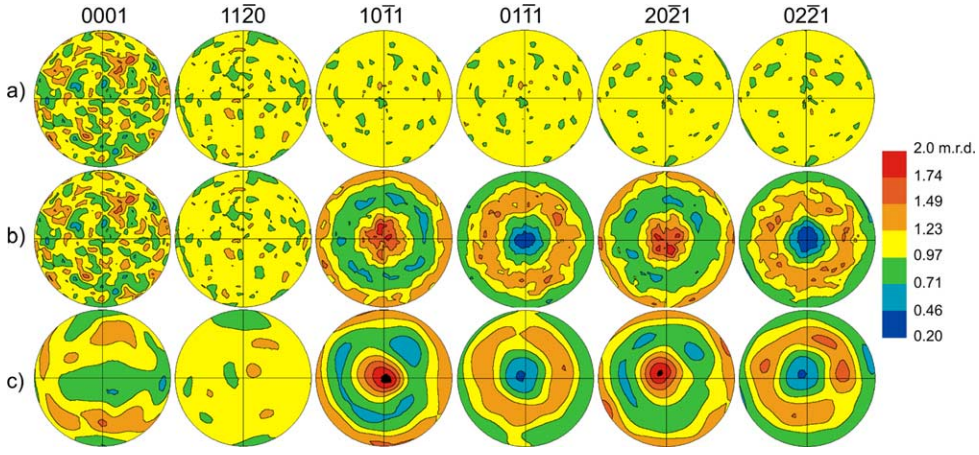

Fig. 8. (a) Pole figures for quartz calculated from 5000 random orientations that were expanded to 10,000 by twinning each orientation. (b) Dauphiné twinning model applied to the random texture (a) by applying an axial compressive stress to the center of the pole figure. (c) Initially random novaculite stressed experimentally and measured with the HIPPO diffractometer. Compression direction at center. Equal area projection, linear scale.

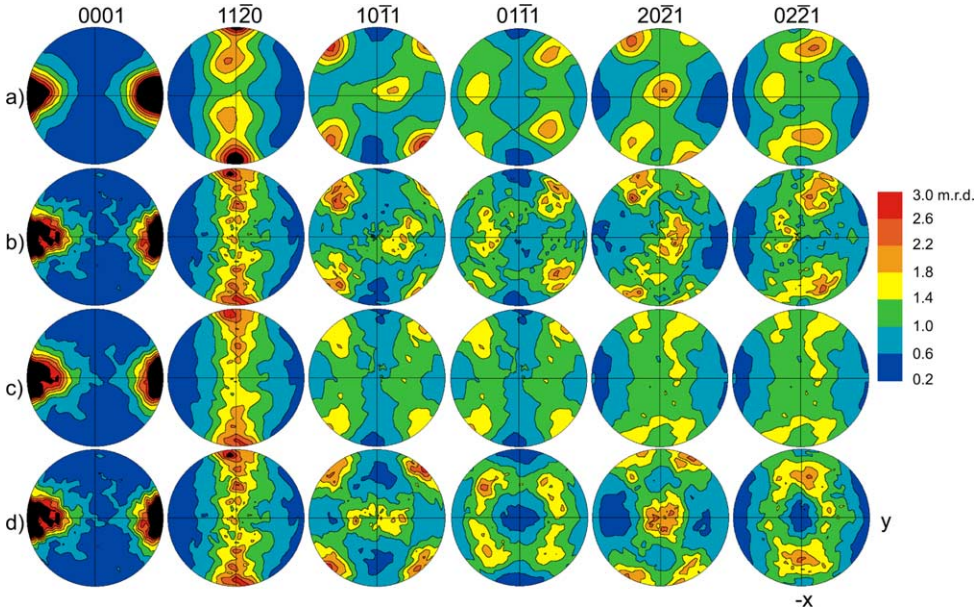

Fig. 9. (a) Pole figures for quartz in sample PC418, slightly rotated compared with Fig. 6 to make it more symmetrical. (b) The ODF of (a) is discretized into 5000 weighted orientations; then (c) Dauphiné twinning is applied to all, producing 10,000 orientations. (d) After applying the Dauphiné twinning algorithm by compressing along the center of the pole figure, the resulting texture is very similar to that observed (b), except for the higher symmetry of rhombohedral pole figures. Equal area projection, linear scale.

Dauphiné twinning in quartz-bearing rocks has indeed a potential as a paleo-piezometer to estimate not only stress directions but also stress magnitudes. Shock waves produced by a meteorite impact may activate Dauphine twinning (Wenk et al., 2005). This example suggests that much lower tectonic stresses are sufficient.

Naturally many uncertainties remain. In most microstructural studies of naturally and experimentally deformed quartzites, Dauphiné twinning has not been observed with the transmission electron microscope (TEM) where identification of twin boundaries is most unambiguous. Even a detailed investigation of Dauphiné twins by Barber and Wenk (1991) revealed no twin boundaries in the experimental samples of Tullis (1970), indicating that in most cases twinning has likely gone to completion. There is more evidence for Dauphiné twinning from scanning electron microscope (SEM) EBSD observations of metamorphic quartzites (e.g. Trimby et al., 1998; Heidelbach et al., 2000; Lloyd, 2000; Wheeler et al., 2003; Piazolo et al., 2005). Clearly a combined TEM, SEM and neutron diffraction study of the same samples should clarify some of the ambiguities.

7. Conclusions

With TOF neutron diffraction and Rietveld data analysis it has become possible to determine quantitatively bulk textures in polymineralic rocks. Quartz mylonites from the Santa Rosa mylonite zone display consistent texture patterns over tens of kilometers, even in the orientation distributions of positive and negative rhombs. Texture differences between rhombs in the same sample can be largely explained by mechanical Dauphiné twinning produced by a stress applied normal to the foliation plane. Our results suggest that Dauphiné twinning in quartz-bearing rocks can reflect regional, tectonic stress distributions and may thus be used as a paleo-piezometrer. This technique may be valuable in sedimentary as well as metamorphic rocks that have been subjected to stress, and should be applied and tested with other quartz textures.

Acknowledgements

We are appreciative for financial support from IGPP-LANL, NSF, DOE-BES and UC-CLC. HRW is thankful for generous hospitality during a sabbatical leave at GFZ Potsdam. We gratefully acknowledge access to the neutron diffraction facilities at LANSCE and support by instrument scientists Sven Vogel and Darrick Williams. LANSCE is funded by the US Department of Energy under Contract W-7405-ENG-36. Constructive and thoughtful reviews by G.E. Lloyd and D.J. Prior have been most valuable.

References

Baker, D.W., Riekels, L.M., 1977. Dauphiné twinning in quartz mylonite. Journal of Geology 80, 15–26.

Baker, D.W., Wenk, H.-R., 1972. Preferred orientation in a low-symmetry quartz mylonite. Journal of Geology 80, 81–105.

Barber, D.J., Wenk, H.-R., 1991. Dauphiné twinning in deformed quartzites: implication of an in situ TEM study of the α–β phase transformation. Physics and Chemistry of Minerals 17, 492–502.

Brigatti, M.F., Davoli, P., 1990. Crystal structure refinement of 1 M plutonic biotites. American Mineralogist 75, 305–313.

Bunge, H.-J., 1982. Texture Analysis in Materials Science—Mathematical Methods. Butterworths, London.

Erskine, B.C., Wenk, H.-R., 1985. Evidence for late Cretaceous crustal thinning in the Santa Rosa mylonite zone, southern California. Geology 13, 274–277.

Gerald, J.D.F., Parise, J.B., MacKinnon, I.D.R., 1986. Average structure of an An48 plagioclase from the Hogarth Ranges. American Mineralogist 71, 1399–1408.

Glinnemann, J., King Jr., H.E., Schulz, H., Hahn, T.H., La Placa, S.J., Dacol, F., 1992. Crystal structures of the low-temperature quartz-type phases of SiO_2 and GeO_2 at elevated pressure. Zeitschrift für Kristallographie 198, 177–212.

Goodwin, L.B., Wenk, H.-R., 1995. Development of phyllonite from granodiorite—mechanisms of grain-size reduction in the Santa Rosa mylonite zone, California. Journal of Structural Geology 17, 689–707.

Groshong, R.H., Teufel, L.W., Gasteiger, C., 1984. Precision and accuracy of the calcite strain-gauge technique. Geological Society of America Bulletin 95, 357–363.

Heidelbach, F., Kunze, K., Wenk, H.-R., 2000. Texture analysis of a recrystallized quartzite using electron diffraction in the scanning electron microscope. Journal of Structural Geology 22, 91–104.

Helming, K., Wenk, H.-R., Choi, C.S., Schäfer, W., 1994. Description of quartz textures by components: examples from metamorphic rocks. In: Bunge, H.J. et al. (Ed.), Texture of Geological Materials. Oberursel, Germany, pp. 303–325.

Le Bail, A., Duroy, H., Fourquet, J.L., 1988. Ab initio structure determination of LiSBWO6 by X-ray powder diffraction. Materials Research Bulletin 23, 447–452.

Lloyd, G.E., 2000. Grain boundary contrast effects during faulting of quartzite: an SEM/EBSD analysis. Journal of Structural Geology 22, 1675–1693.

Lloyd, G.E., 2004. Microsturctural evolution in a mylonitic quartz simple shear zone: the significant roles of dauphine twinning and misorientation. In: Alsop, G.I. et al. (Ed.), Transports and Flow Processes in Shear Zones Special Publication, 224. Geological Society of London, pp. 39–61.

Lloyd, G.E., Kendall, J.-M., 2005. Petrofabric derived seismic properties of a mylonitic quartz simple shear zone: implications for seismic reflection profiling. In: Harvey, P.K. et al. (Ed.), Petrophysical Properties of Crystalline Rocks Special Publication, 240. Geological Society of London, pp. 75–94.

Lutterotti, L., Matthies, S., Wenk, H.-R., 1999. MAUD: a friendly Java program for materials analysis using diffraction. International Union of Crystallography Committee Powder Diffraction Newsletter 21, 14–15.

Matthies, S., 2002. 20 years WIMV, history, experience and contemporary developments. Materials Science Forum 228, 83–88.

Matthies, S., Vinel, G.W., 1982. On the reproduction of the orientation distribution function of textured samples from reduced pole figures using the concept of conditional ghost correction. Physica Status Solidi, B 112, K111–K114.

Matthies, S., Pehl, J., Wenk, H.-R., Lutterotti, L., Vogel, S.C., 2005. Quantitative texture analysis with the HIPPO neutron TOF diffractometer. Journal of Applied Crystallography 38, 273–276.

McSkimin, H.J., Andreatch Jr., P., Thurston, R.N., 1965. Elastic moduli of quartz versus hydrostatic pressure at 25° and −195.8°C. Journal of Applied Physics 36, 1624–1632.

O'Brien, D.K., Wenk, H.-R., Ratschbacher, L., You, Z.D., 1987. Preferred orientation of phyllosilicates in phyllonites and ultramylonites. Journal of Structural Geology 9, 719–730.

Piazolo, S., Prior, D.J., Holness, M., 2005. The use of combined cathodoluminescence and EBSD analysis: a case study investigating grain boundary migration mechanisms in quartz. Journal of Microscopy 217, 152–161.

Rowe, K.J., Rutter, E.H., 1990. Paleostress estimation using calcite twinning—experimental calculation and application to nature. Journal of Structural Geology 12, 1–17.

Sander, B., 1950. Einführung in die Gefügekunde der geologischen Körper. Springer, Vienna.

Schmid, S.M., Casey, M., 1986. Complete fabric analysis of some commonly observed quartz *c*-axis patterns. In: Hobbs, B.E., Heard, H.C. (Eds.), Mineral and Rock Deformation: Laboratory Studies The Paterson Volume. Geophysical Monograph, 36. American Geophysical Union, Washington, DC, pp. 263–286.

Schmid, S.M., Casey, M., Starkey, J., 1981. An illustration of the advantages of a complete texture analysis described by the orientation distribution function (ODF) using quartz pole figure data. Tectonophysics 78, 101–117.

Schubnikow, A., Zinserling, K., 1932. Über die Schlag- und Druckfiguren und über die mechanischen Quarzzwillinge. Zeitschrift für Kristallographie 83, 243–264.

Takeshita, T., Wenk, H.-R., Lebensohn, R., 1999. Development of preferred orientation and microstructure in sheared quartzite: comparison of natural data and simulated results. Tectonophysics 312, 133–155.

Thomas, L.A., Wooster, W.A., 1951. Piezocrescence—the growth of Dauphiné twinning in quartz under stress. Proceedings of the Royal Society of London A 208, 43–62.

Tome, C.N., Lebensohn, R.A., Kocks, U.F., 1991. A model for texture development dominated by deformation twinning: application to zirconium alloys. Metallurgica et Materialia 39, 2667–2680.

Trimby, P.W., Prior, D.J., Wheeler, J., 1998. Grain boundary hierarchy development in a quartz mylonite. Journal of Structural Geology 20, 917–935.

Tullis, J., 1970. Quartz: preferred orientation in rocks produced by Dauphiné twinning. Science 168, 1342–1344.

Tullis, J., Tullis, T., 1972. Preferred orientation of quartz produced by mechanical Dauphiné twinning: thermodynamics and axial experiments. American Geophysical Union Monograph 16, 67–82.

Tullis, T.E., 1980. The use of mechanical twinning in minerals as a measure of shear stress magnitudes. Journal of Geophysical Research 85, 6263–6268.

Wenk, H.-R., 1985. Measurement of pole figures. In: Preferred Orientation in Deformed Metals and Rocks: an Introduction to Modern Texture Analysis, Chapter 2. Academic Press, Orlando, pp. 11–47.

Wenk, H.-R., 1998. Deformation of mylonites in Palm Canyon, California, based on xenolith geometry. Journal of Structural Geology 20, 559–571.

Wenk, H.-R., Pannetier, J., 1990. Texture development in deformed granodiorites from the Santa Rosa mylonite zone, southern California. Journal of Structural Geology 12, 177–184.

Wenk, H.-R., Canova, G., Brechet, Y., Flandin, L., 1997. A deformation-based model for recrystallization of anisotropic materials. Acta Materialia 45, 3283–3296.

Wenk, H.-R., Matthies, S., Donovan, J., Chateigner, D., 1998. Beartex: a Windows-based program system for quntitative texture analysis. Journal of Applied Crystallography 31, 262–269.

Wenk, H.-R., Johnson, L.R., Ratschbacher, L., 2000. Pseudotachylites in the eastern Peninsular Ranges of California. Tectonophysics 321, 253–277.

Wenk, H.-R., Lutterotti, L., Vogel, S., 2003. Texture analysis with the new HIPPO TOF diffractometer. Nuclear Instruments and Methods A515, 575–588.

Wenk, H.-R., Lonardelli, I., Vogel, S.C., Tullis, J., 2005. Dauphiné twinning as evidence for an impact origin of preferred orientation in quartzite: an example from Vredefort, South Africa. Geology 33, 273–276.

Wheeler, J., Jiang, X., Prior, D.J., Tullis, J., Drury, M., Trimby, P.W., 2003. From geometry to dynamics of microstructure: using boundary lengths to quantify boundary misorientations and anisotropy. Tectonophysics 376, 19–35.

Will, G., Bellotto, M., Parrish, W., Hart, M., 1988. Crystal structures of quartz and magnesium germinate by profile analysis of synchrotron-radiation high-resolution powder data. Journal of Applied Crystallography 21, 182–191.

Wooster, W.A., Wooster, N., 1946. Control of electrical twinning in quartz. Nature 157, 405–406.

Young, R.A. (Ed.), 1993. The Rietveld Method. International Union of Crystallography. Oxford University Press, Oxford, UK.